# Supplement of 'Influence of heterogeneous thermal conductivity on the long-term evolution of the lower mantle thermochemical structure: implications for primordial reservoirs'

Joshua M. Guerrero[1], Frédéric Deschamps[1], Yang Li[2], Wen-Pin Hsieh[1], and Paul J. Tackley[3]

[1]Institute of Earth Sciences, Academia Sinica, Taipei
[2]State Key Laboratory of Lithospheric Evolution, Institute of Geology and Geophysics, Institutions of Earth Science, Chinese Academy of Sciences, Beijing
[3]Department of Earth Sciences, ETH Zürich, Zürich

**Correspondence:** Joshua Martin Guerrero (joshua@earth.sinica.edu.tw), Frédéric Deschamps (frederic@earth.sinica.edu.tw)

## Contents of the supplement

## 1   Introduction

Supplement contains Text S1 to S2, which outlines the details of the numerical model and its main characteristics, details regarding converting between potential temperature and full (including the adiabat) temperature, definitions of mantle structures including plume and downwelling regions, and the calculation of derived physical parameters including the average height and the density anomaly profiles associated with thermochemical material, Table S1, listing all parameters and dimensional scale for our simulations, and Figures S1 to S7.

## 2   Text S1 - Details of numerical simulations

We model compressible thermochemical mantle convection using the finite volume code StagYY. The conservation equations of mass, energy, momentum, and composition are solved on a 2D spherical annulus domain (e.g., Hernlund & Tackley, 2008). Details of the numerical techniques used to solve this system may be found in Tackley (2008). All simulations are computed non-dimensionally and can be dimensionalized using input and scaling parameters listed in Table S1. Dimensionalizing temperature requires correcting for adiabatic compression effects and is detailed in Text S2. The main properties of our model are discussed below.

## 2.1 Geometry and general physical properties

Each calculation is performed in a 2D spherical annulus domain, which emulates convection in a variable-thickness slice of a spherical shell centred at the equator. The spherical annulus is characterized with a curvature factor $f = 0.55$ (calculated from the ratio of core-mantle boundary radius to surface radius) and the domain is subdivided into a radial resolution and lateral resolution of 128 and 2048 grid points, respectively. Additional grid refinement is specified at the surface and core-mantle boundaries as well as the 660-km transition to ensure that the flow is well resolved in those regions. The annulus domain features a wrapping side boundaries and free-slip surface and core-mantle boundaries. The surface temperature is defined at 300 K and the core-mantle boundary is defined at 3440 K, which is determined by the reference state (discussed in the next section).

System heating is from the bottom and internal heat sources. In our model, the total internal heating rate is controlled by a reference value, $H$, and accounts for the internal heating rates representative of regular mantle material and primordial material. To account for the possible enrichment of heat-producing elements (HPEs) in primordial material (e.g., Richter, 1985; Kellogg et al., 1999), we adopt a compositional heating ratio (or enrichment factor), $dH_{prim}$, that expresses the internal heating rate of thermochemical piles relative to regular mantle material. The internal heating rate of regular mantle material, $H_M$, (outside of primordial material) is adjusted so that the average internal heating rate of the mantle remains equal to the specified reference value. This internal heating rate is given by

$$H_M = H \times \frac{(1 + C_{total}(dH_{prim} - 1))}{(1 + \bar{C}(dH_{prim} - 1))}, \tag{1}$$

where $C_{total}$ is the total amount and $\bar{C}$ is the average value of primordial material, respectively. For all calculations, we employ a reference internal heating rate $H = 20$, which corresponds to a dimensional value of $5.44 \times 10^{-12}$ Wkg$^{-1}$ and an enrichment factor $dH_{prim} = 10$.

Compressibility also generates sinks and sources of heat that are controlled by the dissipation number, Di, which varies radially and is given by

$$\text{Di}(z) = \frac{\alpha_{\text{ref}}(z)gD}{C_P}, \tag{2}$$

where $z$ is the height above the core-mantle boundary, $\alpha_{\text{ref}}(z)$ is the reference thermal expansivity profile, $g$ is the acceleration due to gravity, $D$ is the mantle thickness, and $C_P$ is the heat capacity (which is assumed constant throughout the system). The surface dissipation number is set to $\text{Di}_{surf} = 1.2$, and the depth variation of thermal expansivity imply a depth average of 0.32.

The fluid properties of the mantle (density, viscosity, thermal diffusivity, and thermal conductivity) are allowed to vary as the system evolves so that the system Rayleigh number is not known *a-priori*. The reference Rayleigh number, $Ra_{\text{ref}}$, which governs the vigour of convection, is evaluated using the surface values of thermodynamic parameters and reference viscosity, $\eta_{\text{ref}}$. We prescribe $Ra_{\text{ref}} = 3 \times 10^8$ for all calculations, which results in effective Rayleigh numbers between $10^6$ and $5 \times 10^6$, depending on the conductivity model.

## 2.2 Reference thermodynamical model

50 Compressible thermochemical convection is characterized by variations relative to a thermodynamic reference state. Reference profiles for the density, temperature, and thermal expansivity are calculated based on the thermodynamic relationships for the Earth's mantle, which are summarized in Tackley (1998). The surface reference temperature, $T_{AS}$, corresponds to a non-dimensional adiabatic temperature of 0.64 (and dimensional value of 1600 K). The reference temperature profile represents a geotherm (which corrects for an adiabatic temperature increase) corresponding to $T_{AS}$. The reference thermal expansivity

55 profile, $\alpha_{ref}(z)$, decreases by a factor of 5 from surface to core. The density increases with depth by a factor of approximately 1.5. The Grüneisen parameter, $\gamma$, varies with depth such that its product with density is constant. Thermal conductivity is calculated separately and the reference conductivity profile depends on the conductivity model employed (see Methods Sect. in the main text). The parameters defining this reference state is listed in the Table S1 is illustrated in Figure S1.

## 2.3 Thermochemical field

60 The thermochemical field distinguishes between regular mantle material and a chemically distinct, primordial, material. The primordial material we consider in our models characterizes chemically distinct heterogeneities at the base of the Earth's mantle as a result of early differentiation. The evolution of thermochemical reservoirs is modelled using the tracer ratio method (Tackley & King, 2003). The number of tracers per cell is 40 so that there are just over 10 million tracers in the spherical annulus domain. Tracers are associated with both regular mantle and primordial material and are advected following a 4th

65 order Runge-Kutta method. The compositional field is inferred from the concentration, $C$, of particles of primordial material in each cell. This field takes on values between 0 for a cell filled with regular material only and 1 for a cell filled with primordial material only. Specifying the exact composition of regular mantle material and primordial material is not needed to calculate the evolution of dense material. Nevertheless, we assume that regular mantle material is pyrolytic and that the primordial material is enriched in iron oxide and bridgmanite.

70 In our models, the initial distribution of primordial material is contained within a uniform layer on top of the CMB with thickness, $h_{DL}$, which corresponds to a volume fraction, $X_{prim}$, by

$$h_{DL} = \frac{[X_{prim}(1-f^3) + f^3]^{1/3} - f}{1 - f}. \tag{3}$$

Using $f = 0.55$, the non-dimensional thickness of the dense layer in our model is 0.05514, which corresponds to the bottom 160 km of the lower mantle and a volume fraction of 3%.

75 Because primordial material is enriched in heavier minerals, it is assumed to be denser than regular (pyrolytic) mantle material. The chemical density contrast between both materials is characterized by a chemical buoyancy ratio, $B$, which is defined with respect to the reference density profile and is given by

$$B = \frac{\Delta \rho_C(z)}{\alpha_S \rho_{ref}(z) \Delta T_S} \tag{4}$$

We prescribe a value of 0.23, which corresponds to a chemical density contrast, $\Delta \rho_C(z)$, of 95 $kgm^{-3}$ near the surface

80 and 152 $kgm^{-3}$ near the CMB. From this definition of the buoyancy ratio, the chemical density contrast increases with depth

3

proportionally to the reference density. Compared with models with $B$ defined with respect to the surface density, the buoyancy ratios required for stable chemical stratification will be smaller.

## 2.4 Viscosity

Viscosity is modelled using an Arrhenius formulation given by

$$85 \quad \eta_M(\tilde{d}, \tilde{T}, C) = \eta_{\text{ref}}[1 + 29H(\tilde{d} - \tilde{d}_{ULM})] \exp\left(V_a\tilde{d} + E_a\frac{1}{\tilde{T} + \tilde{T}_{off}} + \log(\Delta\eta_C)C\right). \quad (5)$$

Depth- dependence is characterized by a viscosity contrast of $10^2$ across the mantle depth (corresponding to a logarithmic vertical viscosity ratio $V_a = 2.3026$). An additional viscosity jump by a factor of 30 is imposed at the 660-km boundary (with non-dimensional depth given by $\tilde{d}_{ULM} = 0.22837$) to account for a phase change (expressed by the Heaviside function in Equation 5). Temperature- dependence is characterized by a thermal viscosity contrast of $10^7$ (corresponding to a logarithmic thermal viscosity ratio $E_a = 20.723$). The parameter $\tilde{T}_{off}$ is a temperature offset, which is added to the temperature to reduce the viscosity contrast across the top thermal boundary layer. In this study, $\tilde{T}_{off} = 0.90$. A factor of 30 viscosity contrast ($\Delta\eta_C$) is imposed between lower mantle material and thermochemical reservoirs because dense material enriched in bridgmanite (Trampert et al., 2004; Mosca et al., 2012) is assumed to be more viscous (Yamazaki & Karato, 2001).

A yield stress, $\sigma_0$, of 290 MPa is imposed at the surface so that the development of a stagnant-lid is avoided. The yield viscosity is defined from the yield stress $\sigma_Y = \sigma_0 + \dot{\sigma}_z P$ and the second invariant of the stress tensor, $\dot{e}$, and is given by

$$\eta_Y = \frac{\sigma_0 + \dot{\sigma}_z P}{2\dot{e}}. \quad (6)$$

The total viscosity then is given by

$$\eta = \frac{1}{\frac{1}{\eta_M} + \frac{1}{\eta_Y}} \quad (7)$$

Finally, viscosity is truncated so that non-dimensional viscosity values do not exceed $10^5$ or fall below $10^{-3}$ of the reference viscosity.

## 2.5 Phase changes

The transformation of ringwoodite into bridgemanite and ferropericlase at 660 km is modelled with a discontinuous phase transition controlled by defining a point on the phase boundary and a Clapeyron slope, $\Gamma_{660}$. Here, the anchor point is set at $d = 660$ km and $T = 1900$ K, and the Clapeyron slope is set to $\Gamma_{660} = -2.5$ MPaK$^{-1}$. The accompanying density contrast is fixed to $\Delta\rho_{660} = 400$ kgm$^{-3}$ and is scaled with the surface density. Combined with the 660-km viscosity increase (from upper to lower mantle), the 660-km phase change has a strong influence on the geometry of the plumes. This transition acts as a negatively buoyant barrier, which results in a spreading of the plume conduit beneath this boundary, and a thinning above it. Further phase changes in the lowermost mantle from perovskite to post-perovskite is neglected.

## 2.6 Initial conditions

The initial condition for the temperature field is based on an adiabatic temperature of 2000 K with surface and core-mantle boundary layer thicknesses of approximately 30 km. Random temperature perturbations with an amplitude of 125 K are uniformly distributed throughout the domain. Under this setup, an initial transient phase lasting approximately 1.0 to 2.0 Gyr is observed (depending on the conductivity model employed) where the bottom of the mantle heats up and the first downwellings impinge on the initial dense layer.

Simulations are computed over a non-dimensional time of 0.0318. Dimensionalizing using the diffusion timescale ($D^2/\kappa_S$), results in a total of 11.2 Gyr. The longer simulation time is necessary to allow the simulations' heat flows to achieve a quasi-steady state. It is possible that significant developments during the long-term evolution of thermochemical material may occur over timescales comparable to or longer than the age of the solar system. We point out that our models are not designed to model the detailed evolution of the Earth's mantle, for which accurate initial conditions are not yet known. Instead, our models aim to identify the thermochemical structure and its evolution as a function of the system's conductivity model.

## 3 Text S2 - Derived quantities and statistics on observed physical parameters

### 3.1 Adiabatic correction and rescaling to Earth's mantle

The energy and momentum equations are solved with the temperature field that has been corrected for adiabatic effects. However, for practical reasons, the output temperature field states are saved as the uncompressed temperature, which excludes these effects. In all figures that present temperature fields, plume and downwelling contours, or temperature profiles (Figures 2, 3 and 4 in the main text and Supplement Figures S1 to S7), temperature has been rescaled and corrected with the adiabatic increase of temperature with pressure. The dimensional temperature field, $T(x, y, z)$, is obtained from the non-dimensional, uncompressed temperature field, $\tilde{T}(x, y, z)$, following

$$T(x,y,z) = [\tilde{T}(x,y,z) + \tilde{T}_{top}] \times a(z)\Delta T_S \tag{8}$$

where $\Delta T_S = 2500$ K is the superadiabatic temperature difference, $\tilde{T}_{top}$ is the non-dimensional surface temperature, which is fixed to 0.12 and corresponds to a surface temperature $T_{surf} = 300$ K, and $a(z)$ is the adiabatic correction at height $z$ above the core-mantle boundary. The adiabatic correction is given by

$$a(z) = \exp\left[\int_0^z \mathrm{Di}_{surf} \frac{\alpha_{\mathrm{ref}}(z')}{C_{P\mathrm{ref}}(z')} dz'\right] \tag{9}$$

where $\mathrm{Di}_{surf}$ is the surface dissipation number, and $\alpha_{\mathrm{ref}}(z)$ and $C_{P\mathrm{ref}}(z)$ are the thermodynamic reference thermal expansivity and heat capacity, respectively. The adiabatic correction varies from 1.0 at the surface to about 1.40 at the CMB.

## 3.2 Definition of mantle structures

Mantle structures, namely thermal upwellings and downwellings, are indicated in the various field snapshots we present in our figures. These structures can be particularly helpful when the field shows no discernible variations that might indicate flow (i.e., a constant or radially varying conductivity field). The contour of an upwelling characterizes mantle plumes and similarly, the contour of a downwelling characterizes subducting slabs. We adapt the definition of thermal structures based on the formalism by Labrosse (2002). Here, the plume region is defined as regions where the temperature exceeds the horizontally averaged temperature, $\bar{T}(z)$, by a fraction of $c_{plume}$ of the maximum excess temperature anomaly. That is, regions where temperature is given by

$$T_{plume}(z) \geq \bar{T}(z) + c_{plume}[T_{max}(z) - \bar{T}(z)], \tag{10}$$

where $T_{max}(z)$ is the maximum temperature. Downwelling regions are defined similarly and given by

$$T_{slab}(z) \leq \bar{T}(z) + c_{slab}[T_{min}(z) - \bar{T}(z)], \tag{11}$$

where $T_{min}(z)$ is the minimum temperature. The values of $c_{plume}$ and $c_{slab}$ are subjective and decreasing these constants increase the regions they characterize. In this study, both $c_{plume}$ and $c_{slab}$ are set to 0.5 so that the regions are defined by half the magnitude of the difference between the temperature anomaly and the horizontal average.

Thermochemical piles are defined by a threshold value of $C$. In our calculations, we define thermochemical piles as having $C$ larger than 0.9. The higher threshold value means that piles, as their name suggests, are the densest material that pool on top of the CMB. Even the densest material in our calculations exhibit greater extension above the CMB. Furthermore, a lower threshold value for thermochemical material may result in estimates of the mean pile temperature that are offset by cooler and lighter material.

## 3.3 Derived quantities

In this study, all observable physical parameters are averaged over a 2 Gyr window centred about $t = 4.5$ Gyr (illustrated in Figure 2 and are presented in Table 1 in the main text). We derive some additional physical parameters such as average height and the mean density anomalies of primordial material below.

The average height of primordial material, $h_C$, is considered as an indication of efficient mixing of primordial material in the mantle. This height is calculated using a volumetric integral weighted by the concentration of primordial material,

$$h_C = \int_V (r - r_{cmb}) C(r, \theta, \phi) dV \Bigg/ \int_V C(r, \theta, \phi) dV. \tag{12}$$

Average height of primordial material is bound from below by a minimum value, $h_{C,min} = h_{dl}/2$, where $h_{dl}$ is the initial thickness of the thermochemical reservoir, and bound from above by a maximum value (when primordial material is completely

mixed) is given by

$$h_{C,max} = \frac{\left(\frac{1+f^3}{2}\right)^{1/3} - f}{1 - f}. \tag{13}$$

Here, $h_{C,min} = 0.028$ and $h_{C,max} = 0.634$, which corresponds to dimensional heights 80 and 1830 km, respectively. We also consider other mean heights of primordial material for $C(r,\theta,\phi)$ within specific ranges. Minor enrichment of dense material with $C(r,\theta,\phi) \leq 0.02$ is useful for monitoring the onset of slow mixing of primordial material into regular mantle material. A moderate enrichment of dense material with $C(r,\theta,\phi) \leq 0.90$ and $> 0.02$ is useful for monitoring the rapid entrainment of primordial material. This value range characterizes a thin veneer of primordial material with $C(r,\theta,\phi) \leq 0.90$ that surrounds the thermochemical reservoirs. The rapid uplift of this material typically precedes the onset of entrainment. Finally, dense material with $C(r,\theta,\phi) > 0.90$ characterizes the thermochemical piles. While some of this material can be rapidly entrained, the bulk concentration will be localized near the CMB. The timing of the onset of the entrainment of dense material, $t_{inst.}$, can be computed from the timing of the maximum of the second derivative of $h_{C \leq 0.9}$ and is confirmed by observing the deviation of $h_{C \leq 0.9}$ from $h_{C \geq 0.9}$ or $h_C$ from $h_{C \geq 0.9}$.

The density anomalies of primordial material, $(d\rho/\rho)_{z,prim}$, is calculated relative to the horizontally averaged density. At each depth in the mantle, the density difference of the primordial field is calculated ($d\rho = \rho_{prim} - \bar{\rho}_z$). The average density anomaly is calculated with respect to the density value of each point at a given depth so that

$$(d\rho/\rho)_{z,prim} = \int_{S_z} \frac{\rho_{prim} - \bar{\rho}_z}{\rho_{prim}} dS_z \Big/ \int_{S_z} dS_z. \tag{14}$$

Monitoring the density profile of primordial material clarifies its distribution throughout the mantle depth. In conjunction with the evolution of average heights, the regions of dense material enrichment is further clarified.
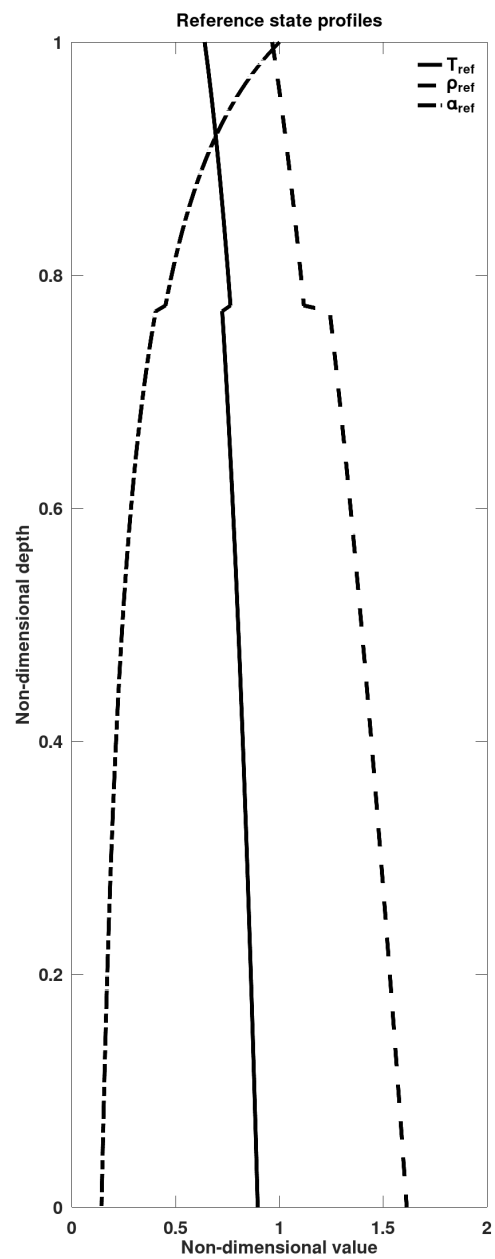
**Figure S1.** Radial profiles for adiabatic temperature, density, and thermal expansivity indicate the reference state for each calculation.

| Parameter | Symbol | Value | Units | Non-dimensional |
|---|---|---|---|---|
| *Non-dimensional parameters* | | | | |
| Reference Rayleigh number | $Ra_{\text{ref}}$ | | | $3.0 \times 10^8$ |
| Surface dissipation number | $Di_{surf}$ | | | 1.2 |
| Total internal heating | $H$ | $5.44 \times 10^{-12}$ | (Wkg$^{-1}$) | 20 |
| Compositional heating ratio | $dH_{prim}$ | | | 10 |
| | | | | |
| *Compositional parameters* | | | | |
| Buoyancy ratio | $B$ | | | 0.23 |
| Volume fraction of dense material (%) | $X_{prim}$ | | | 3% |
| Thickness of initial dense layer | $h_{DL}$ | | | 0.05514 |
| | | | | |
| *Physical & thermodynamical parameters* | | | | |
| Acceleration of gravity | $g$ | 9.81 | (ms$^{-2}$) | 1 |
| Mantle thickness | $D$ | 2891 | (km) | 1 |
| Reference adiabat | $T_{AS}$ | 1600 | (K) | 0.64 |
| Super-adiabatic temperature difference | $\Delta T_S$ | 2500 | (K) | 1 |
| Surface density | $\rho_S$ | 3300 | (kgm$^{-3}$) | 1 |
| Surface thermal expansion | $\alpha_S$ | $5.0 \times 10^{-5}$ | (K$^{-1}$) | 1 |
| Surface thermal diffusivity | $\kappa_S$ | $7.5 \times 10^{-7}$ | (m$^2$s$^{-1}$) | 1 |
| Heat capacity | $C_P$ | 1200 | (Jkg$^{-1}$K$^{-1}$) | 1 |
| Surface conductivity | $k_S$ | 3 | (Wm$^{-1}$K$^{-1}$) | 1 |
| Surface Grüneisen parameter | $\gamma_S$ | | | 1.091 |
| Density jump at z = 660 km | $\Delta\rho_{660}$ | 400 | (kgm$^{-3}$) | 0.1212 |
| Clapeyron slope at z = 660 km | $\Gamma_{660}$ | -2.5 | (MPaK$^{-1}$) | -0.0668 |
| CMB temperature | $T_{CMB}$ | 3440 | (K) | 1.376 |
| Density jump at CMB | $\Delta\rho_{CMB}$ | 5280 | (kgm$^{-3}$) | 1.6 |
| | | | | |
| *Conductivity Parameters* | | | | |
| Depth- dependence contrast | $K_D$ | | | 1.0 - 10.0 |
| Temperature- dependence exponent | $n$ | | | 0.0, 0.5, 0.8 |
| Compositional correction | $K_C$ | | | 0.5 - 1.0 |
| | | | | |
| *Viscosity Law* | | | | |
| Reference viscosity | $\eta_{\text{ref}}$ | $4.346 \times 10^{20}$ | Pa $\cdot$ s | 1 |
| Viscosity ratio at z = 660 km | $\Delta\eta_{660}$ | | | 30 |
| Logarithmic thermal viscosity ratio | $E_a (= \log(\Delta\eta_T))$ | | | 20.723 |
| Logarithmic vertical viscosity ratio | $V_a (= \log(\Delta\eta_D))$ | | | 2.3026 |
| Compositional viscosity ratio | $\Delta\eta_C$ | | | 30 |
| Surface yield stress | $\sigma_0$ | 290 | (MPa) | $7.5 \times 10^6$ |
| Yield stress gradient | $\dot{\sigma}_z$ | | (PaPa$^{-1}$) | 0.01 |

**Table S1.** Parameters and dimensional scales for our thermochemical mantle convection model.
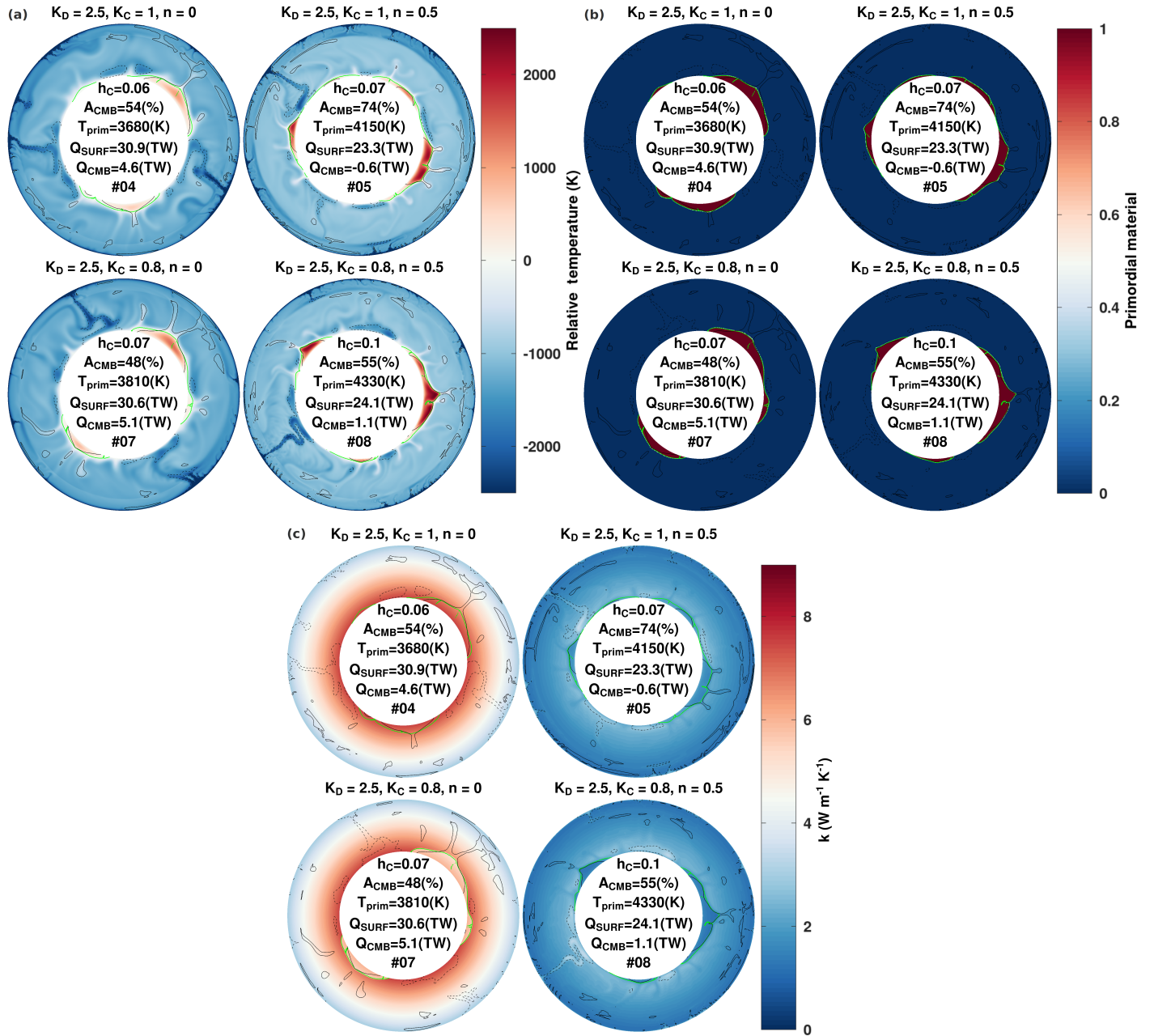
**Figure S2.** Temperature (a), primordial material (b), and conductivity fields (c) corresponding to cases in Figure 2.
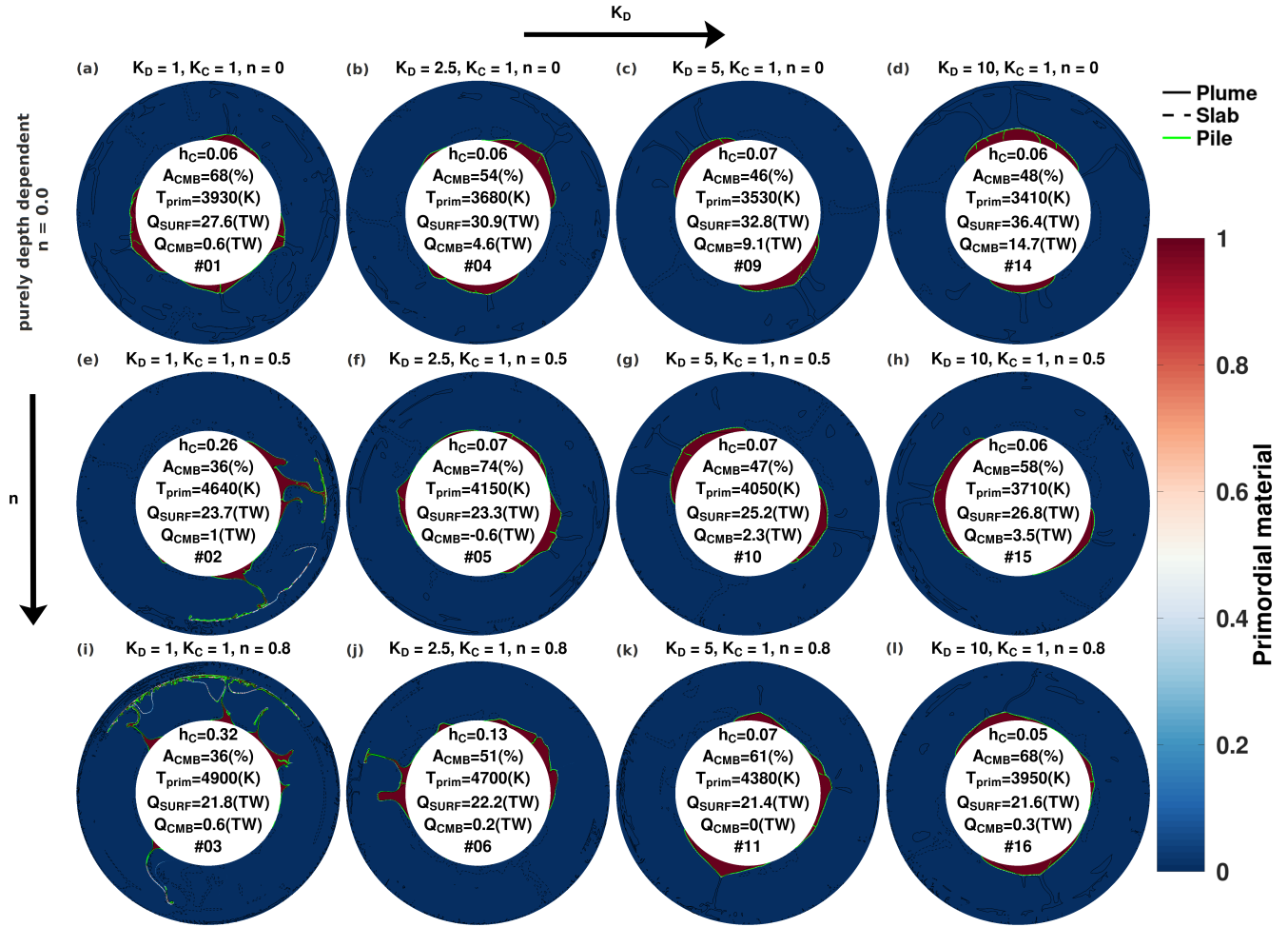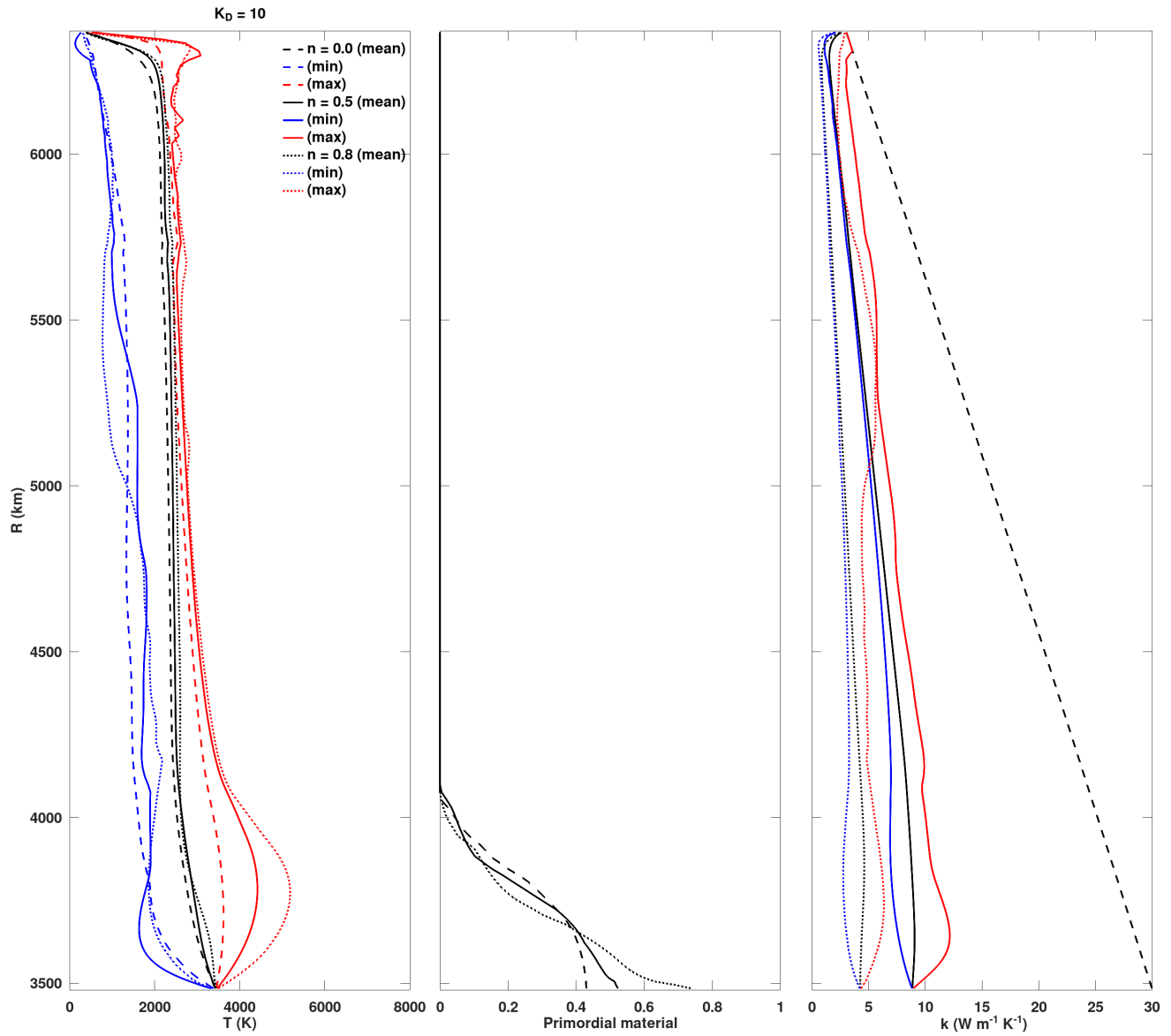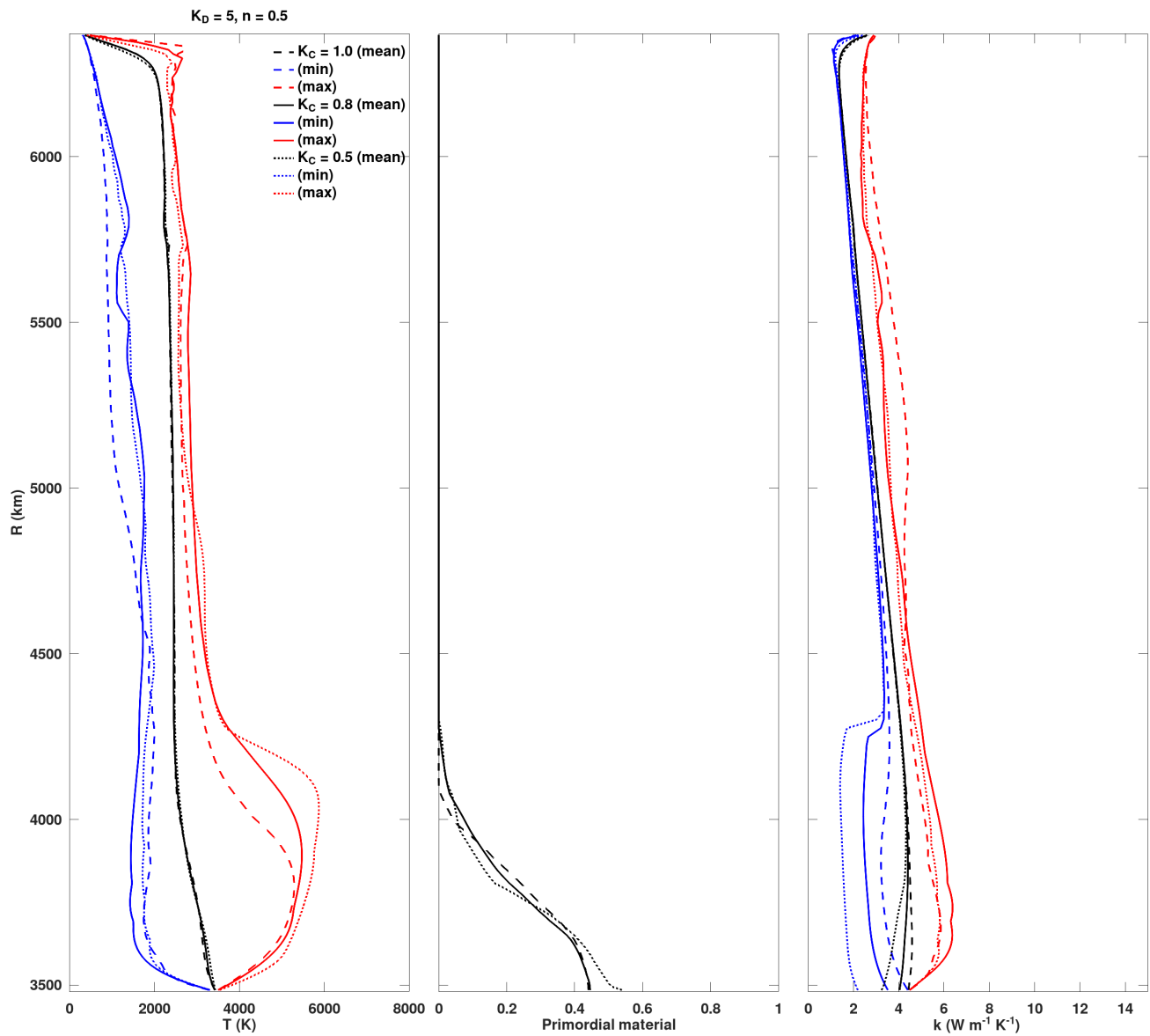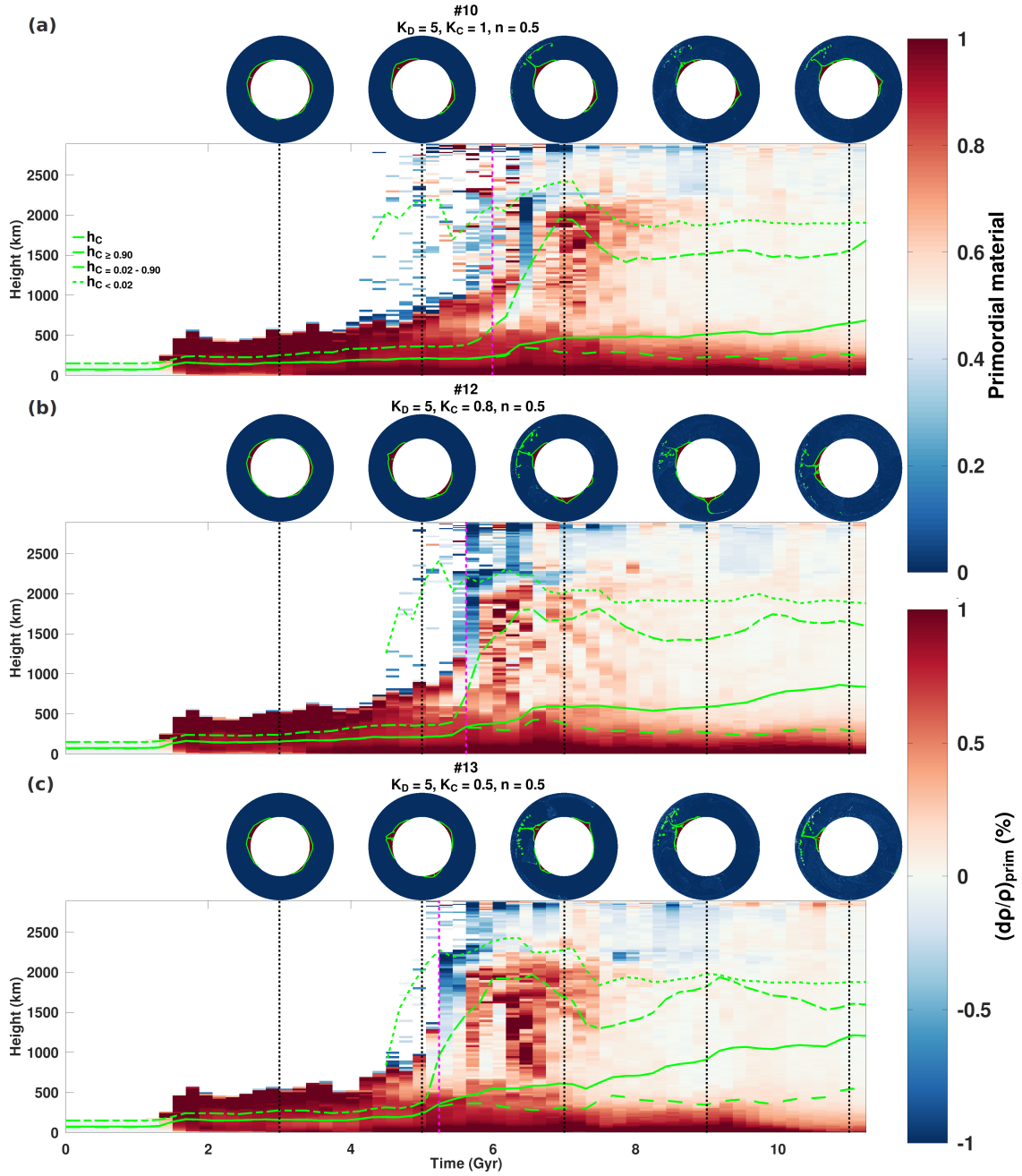
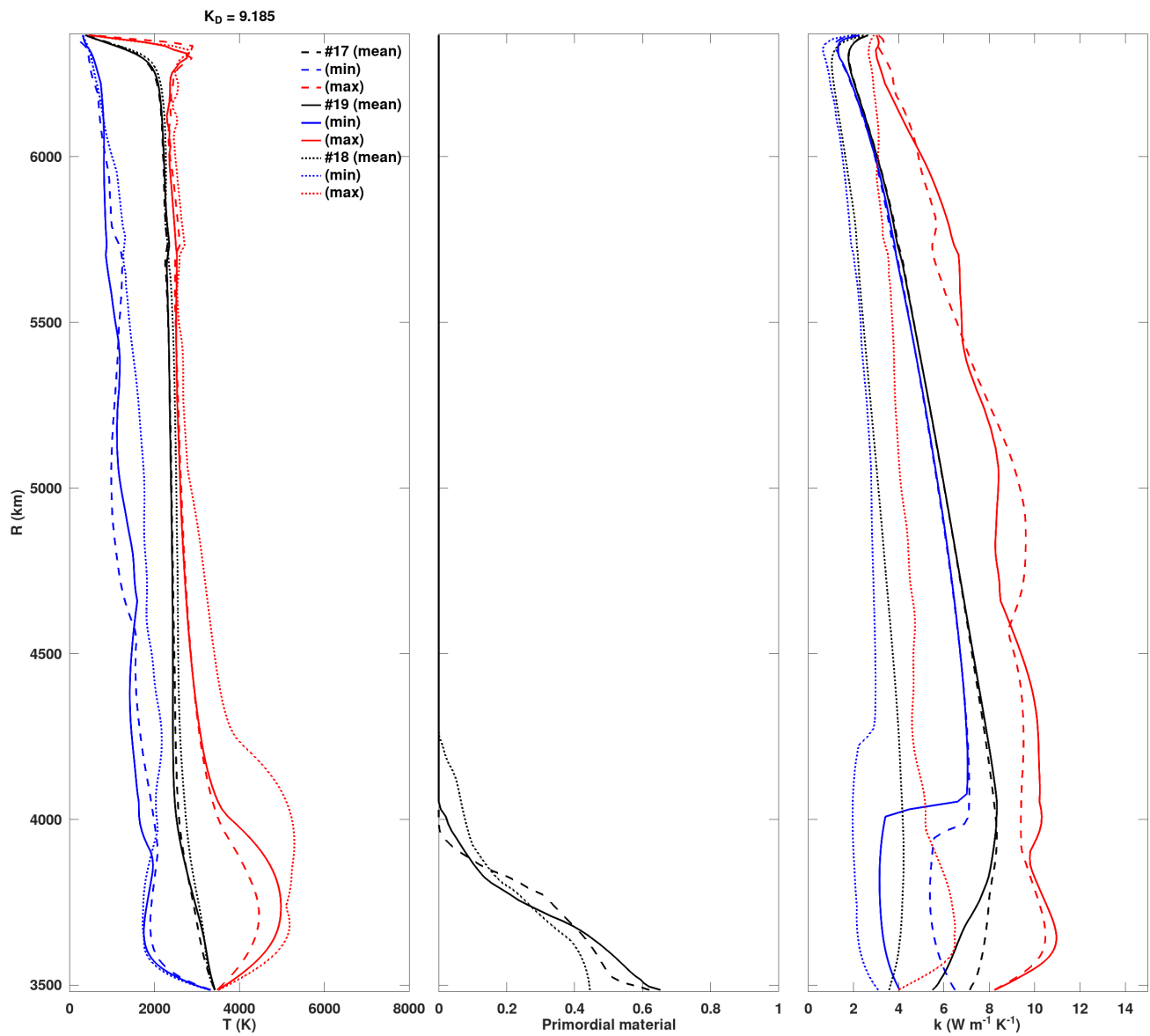**Figure S3.** Primordial material fields corresponding to cases in Figure 3.

**Figure S4.** Mean temperature, primordial material, and composition profiles corresponding to $K_D = 10$ cases in Figures 3 and 4.

**Figure S5.** Mean temperature, primordial material, and composition profiles corresponding to cases in Figure 5.

**Figure S6.** Evolution of the horizontally averaged primordial material density anomalies is illustrated for cases featuring $K_D = 5$ and $n = 0.5$. Primordial field snapshots are sampled at 2 Gyr intervals starting at 3 Gyr above the timeseries (dashed-black vertical line indicates the time). Mean heights of primordial material are plotted on top of the density anomaly timeseries. The dashed-magenta vertical line indicates the onset of instability in thermochemical reservoirs. Piles are indicated similarly as in Figure 5.

**Figure S7.** Mean temperature, primordial material, and composition profiles corresponding to cases in Figure 6.

# References

Hernlund, J. W., & Tackley, P. J. 2008. Modeling mantle convection in the spherical annulus. Physics of the Earth and Planetary Interiors, 171(1-4), 48-54.

185  Kellogg, L. H., Hager, B. H., & van der Hilst, R. D. 1999. Compositional stratification in the deep mantle. Science, 283(5409), 1881-1884.

Klemens, P. G. 1960. Thermal resistance due to point defects at high temperatures. Physical review, 119(2), 507.

Labrosse, S. 2002. Hotspots, mantle plumes and core heat loss. Earth and Planetary Science Letters, 199(1-2), 147-156.

Mosca, I., Cobden, L., Deuss, A., Ritsema, J., & Trampert, J. 2012. Seismic and mineralogical structures of the lower mantle from probabilistic tomography. Journal of Geophysical Research: Solid Earth, 117(B6).

190  Richter, F. M. 1985. Models for the Archean thermal regime. Earth and Planetary Science Letters, 73(2-4), 350-360.

Tackley, P. J. 1998. Three-dimensional simulations of mantle convection with a thermo-chemical basal boundary layer: D. The Core-Mantle Boundary Region, Geodyn. Ser, 28, 231-253.

Tackley, P. J. 2008. Modelling compressible mantle convection with large viscosity contrasts in a three-dimensional spherical shell using the yin-yang grid. Physics of the Earth and Planetary Interiors, 171(1), 7-18.

195  Tackley, P. J., & King, S. D. 2003. Testing the tracer ratio method for modeling active compositional fields in mantle convection simulations. Geochemistry, Geophysics, Geosystems, 4(4).

Trampert, J., Deschamps, F., Resovsky, J., & Yuen, D. 2004. Probabilistic tomography maps chemical heterogeneities throughout the lower mantle. Science, 306(5697), 853-856.

Xu, Y., Shankland, T. J., Linhardt, S., Rubie, D. C., Langenhorst, F., & Klasinski, K. 2004. Thermal diffusivity and conductivity of olivine,
200  wadsleyite and ringwoodite to 20 GPa and 1373 K. Physics of the Earth and Planetary Interiors, 143, 321-336.

Yamazaki, D., & Karato, S. I. 2001. Some mineral physics constraints on the rheology and geothermal structure of Earth's lower mantle. American Mineralogist, 86(4), 385-391.